ADVANCES IN ATMOSPHERIC SCIENCES, VOL. 36, APRIL 2019, 378–396

• **Original Paper** •

Interannual Salinity Variability in the Tropical Pacific in CMIP5 Simulations

Hai ZHI[1], Rong-Hua ZHANG[*2,3,4], Pengfei LIN[4,5], and Peng YU[6]

[1]*College of Atmospheric Sciences, Nanjing University of Information Science and Technology, Nanjing* 210044*, China*

[2]*Key Laboratory of Ocean Circulation and Waves, Institute of Oceanology, Chinese Academy of Sciences, Qingdao* 266071*, China*

[3]*Laboratory for Ocean and Climate Dynamics, Qingdao National Laboratory for Marine Science and Technology, Qingdao* 266237*, China*

[4]*University of Chinese Academy of Sciences, Beijing* 100029*, China*

[5]*State Key Laboratory of Numerical Modeling for Atmospheric Sciences and Geophysical Fluid Dynamics (LASG), Institute of Atmospheric Physics (IAP), Chinese Academy of Sciences, Beijing* 100029*, China*

[6]*The Cooperative Institute for Climate and Satellites (CICS), University of Maryland, College Park, MD* 20740*, USA*

(Received 21 December 2017; revised 25 November 2018; accepted 4 December 2018)

ABSTRACT

Salinity variability and its causes in the tropical Pacific are analyzed using observations, reanalysis products and model simulations. The mixed-layer salinity (MLS) budget analyses from observations and reanalysis products indicate that its interannual evolution is closely related to ENSO and is predominantly governed by surface forcing and surface advection in the western-central equatorial Pacific. It is found that the observed MLS tendency leads Niño3.4 by about 12 months due to the effect of negative freshwater flux (evaporation minus precipitation). These observation-based analyses are used to evaluate the corresponding simulation using GFDL-ESM2M. It is evident that the model can simulate the spatiotemporal variations of MLS with some discrepancies compared to observations. In the warm pool of the equatorial Pacific the MLS tendency in the model is sensitive to ocean dynamics, however model biases cause the tendency to be underestimated. In particular, the freshwater flux is overestimated while the ocean surface zonal current and vertical velocity at the base of the mixed layer are underestimated. Due to model biases in representing the related physics, the effects of surface forcing on the simulated MLS budget are overestimated and those of subsurface and surface advection are relatively weak. Due to weaker surface advection and subsurface forcing than observed, the simulated compensations for surface forcing are suppressed, and the simulated MLS tendency that leads Niño3.4 by 8–10 months, which is shorter than the observed lead time. These results are useful for the interpretation of observational analyses and other model simulations in the tropical Pacific.

Key words: mixed-layer salinity, salt budget, interannual variability, tropical Pacific, model simulation

Citation: Zhi, H., R.-H. Zhang, P. F. Lin, and P. Yu, 2019: Interannual salinity variability in the tropical Pacific in CMIP5 simulations. *Adv. Atmos. Sci.*, **36**(4), 378–396, https://doi.org/10.1007/s00376-018-7309-1.

Article Highlights:

- The MLS budget indicate that its interannual evolution is related to ENSO and governed by surface forcing in the western-central equatorial Pacific.
- The observed MLS tendency leads Niño3.4 by about 12 months due to the effect of negative freshwater flux.
- The model can simulate the spatiotemporal variations of MLS with some discrepancies compared to observations.

1. Introduction

As a tracer of the water cycle, ocean salinity, along with ocean temperature, is a fundamental ocean state variable. While continued efforts have improved our understanding of climate change, the dimensions of this research have expanded to explore the roles of climate phenomena that are associated with salinity variability (Schmitt, 1990; Webster, 1994). Numerous studies have been performed that use information on modeled/observed salinity changes to assess global/regional water cycle change (e.g., Ren and Riser, 2009; Durack et al., 2012; Terray et al., 2012; Katsura et al., 2013; Vinogradova and Ponte, 2013; Skliris et al., 2014). At interannual scales, salinity and the related physics have an important impact on the ENSO-related large-scale climate variability by modifying the oceanic density that feeds back to sea surface temperature (SST) (Zhang and Busalacchi, 2009). And through its role in ENSO, salinity exerts a pronounced influence on climate and weather around several regions and even the globe (e.g., Yu et al., 2014; Yan et al., 2017a,b).

* Corresponding author: Rong-Hua ZHANG
Email: rzhang@qdio.ac.cn

In the tropical Pacific, evident relationships exist between SST variability and the mixed-layer salinity (MLS) (Vialard et al., 2002). For example, the MLS variability can create a "barrier layer" (Lukas and Lindstrom, 1991) by modulating the mixed-layer depth and therefore suppress/enhance upper-ocean temperature and affect the spatiotemporal evolution of the western Pacific warm pool (Sprintall and Tomczak, 1992). In particular, during El Niño, the appearance of a positive barrier layer thickness anomaly in the central-western tropical Pacific restrains the deep cool/salt water from entering into the warm/fresh water of the upper layer, acting as a trap for upper-ocean heat in the tropical Pacific (Da-Allada et al., 2014). MLS variations and the associated oceanic physics, which are intrinsically connected to the dynamics of ENSO, provide a critical feedback to surface temperature in the evolution of ENSO events (Zhang et al., 2010; Zheng et al., 2014). Furthermore, large positive MLS anomaly events occur prior to El Niño, while negative MLS anomaly events appear prior to La Niña (Zheng and Zhang, 2012; Zhu et al., 2014; Zhang et al., 2015). Subsequently, MLS can provide an essential precondition for ENSO's onset and growth (Yim et al., 2008).

Salinity is controlled by its conservation equation, and its budget results from ocean and atmosphere influences (Zhang and Busalacchi, 2009). Several studies have argued that MLS variations have complicated patterns in response to factors such as surface and subsurface forcing and ocean currents (e.g., Delcroix et al., 2011; Singh et al., 2011; Zhang et al., 2012; Vinogradova and Ponte, 2013; Qu et al., 2014; Ponte and Vinogradova, 2016). For example, the MLS variability is very sensitive to the surface advection by the mean oceanic circulation in the heavy precipitation domain at the east edge of the warm pool and especially over the Intertropical Convergence Zone (ITCZ) and South Pacific Convergence Zone (SPCZ) (Vialard and Delecluse, 1998). During the past decade, several studies have focused on the salinity budget of the tropical regions of the ocean (e.g., Delcroix et al., 2005; Mignot et al., 2007; Dong et al., 2009; Bingham et al., 2010; Da-Allada et al., 2015). The MLS budget reveals the robust interannual variability as a result of the influences from surface forcing, advection, and vertical entrainment and mixing in the tropical Pacific (Gao et al., 2014). For example, in the equatorial Pacific, the ENSO-related freshwater forcing changes are responsible for generating and maintaining large MLS anomalies, whereas the MLS variability mainly depends on the surface advection of eastward propagating fresh water in the fresh pool to the central-eastern basin of the Pacific (Hasson et al., 2013).

Notably, simulating salinity is a challenging issue, though substantial improvements in global models have been made over the past decade. Since a standard experimental protocol and an infrastructure were provided in the Coupled Model Intercomparison Project (CMIP), scientists have been able to systematically analyze model simulations to promote model developments and study climate change (Taylor et al., 2012). An assessment of CMIP3 showed that the global coupled models involved could capture well the historical trend of global mean MLS in spite of regional MLS biases as high as ±2.5 practical salinity units (psu) (Terray et al., 2012). Furthermore, as to the salinity signature associated with ENSO in the 23 models of CMIP5, the spatial distribution displays a negative sea surface salinity anomaly in the west of the equatorial band and a positive one in the SPCZ during El Niño, while the opposite is true during La Niña (Delcroix et al., 2011). However, the simulated sea surface salinity variability in the SPCZ tends to be located too far to the east compared with observation. In addition, comparisons of modeled and observed estimates of the surface forcing associated with terms of the salinity budget suggest that model biases in surface forcing are a main factor that induces ocean salinity uncertainty in the tropical Pacific in coupled models (Lin, 2007; Zhang and Busalacchi, 2009).

New fully coupled terrestrial carbon and nutrient cycling Earth system models have been developed by GFDL over the last several years, and were included in CMIP5. They provide all the core simulations within the CMIP5 suite of experiments and can be used to examine the interplay among different components or the climate system response to changes in natural and anthropogenic forcings (Dunne et al., 2012). Among these models, GFDL-ESM2M might better represent climate variability and change related to its variability of surface temperature compared to those in current reanalysis data and other models (Dunne et al., 2012, 2013). Many studies have utilized the CMIP5 results of GFDL-ESMs to evaluate model performance. The crucial role of model dynamics in climate variability is highlighted by the GFDL-ESM2M-simulated ENSO. For example, Langford et al. (2014) found that GFDL-ESM2G has a better ability to simulate the higher climatological precipitation in southwestern North America than current reanalysis products and other models. However, comparison of 23 models from CMIP5 in terms of sea surface salinity and freshwater flux (evaporation minus precipitation) variability demonstrated that GFDL-ESM2M can provide a relatively reasonable spatial distribution despite some discrepancies with the available reanalysis data in the tropical Pacific (Zhi et al., 2015).

Observations and reanalysis products are used to quantitatively illustrate the relationship between salinity variability and its budget terms during ENSO. Therefore, based on the interannual MLS anomaly and its budget in the tropical Pacific, this paper further aims to assess the performance of GFDL-ESM2M with respect to salinity simulations. It is organized as follows: Section 2 describes the methods, validation data and model utilized to study MLS. Section 3 examines MLS and its budget based on the GFDL-ESM2M simulations. A summary and discussion of our work is presented in section 4.

2. Model, validation data, and methods

2.1. *Validation data*

In this paper, the following observational and reanalysis datasets are utilized. The ocean salinity data are long-term

monthly mean gridded data, with a horizontal resolution of $1^\circ \times 1^\circ$ and 42 vertical levels down to a depth of 5000 m, from 1900 to the present day, derived from the objective analysis ensemble dataset (Good et al., 2013) provided by the Met Office Hadley Centre. The SST data are from the ERSST.v4 monthly analysis (Huang et al., 2015), with a $2.0^\circ \times 2.0^\circ$ horizontal resolution and covering the period from January 1854 to the present day. The precipitation data are from GPCP (Adler et al., 2003), with coverage from 1979 to the present day and a $2.5^\circ \times 2.5^\circ$ horizontal resolution. The evaporation data are from the monthly OAFlux dataset (Yu and Weller, 2007), with a horizontal resolution of $1^\circ \times 1^\circ$ and coverage from 1958 to the present day. The ocean zonal, meridional and vertical velocities are from GODAS (Behringer et al., 1998), covering the period from 1979 to the present day and with a horizontal resolution of $1^\circ \times 1^\circ$ grid and 40 vertical levels.

These datasets are regridded to a regular $1^\circ \times 1^\circ$ horizontal grid when needed, via bilinear interpolation. To analyze the natural variability of the climate system and comprehensively consider the valid length of the data, the period for the observational and reanalysis data is selected as 1980–2010. Prior to using the data, we remove the linear trend of the raw data. By doing so, the influence on the climate system due to global warming can be reduced. The statistical significance of relationships in this study is tested with the Student's *t*-test at the 95% confidence level. Besides, in order to remove the intraseasonal characteristics, the time series are additionally applied with an 11-month running mean filter to obtain the interannual anomaly fields.

2.2. *Model*

The GFDL, which constructed the first Earth system models to advance our understanding of Earth's biogeochemical cycles, has completed all of its integrations with GFDL-ESM2M and GFDL-ESM2G for the CMIP5 protocol. The model components of GFDL-ESM2M are briefly described below; a more comprehensive description can be found in Dunne et al. (2012, 2013).

Based on an atmospheric circulation model coupled with an oceanic circulation model, GFDL-ESM2M contains representations of land, sea ice and iceberg dynamics, with its individual components linked by exchange fluxes across interfaces of its component models. The atmospheric component is Atmospheric Model, version 2, which is virtually identical to the Climate Model 2.1 (CM 2.1), with a 2° latitude ×2.5° longitude horizontal D grid using finite-volume advection and 24 vertical levels (Lin, 2004). The ocean component of GFDL-ESM2M adopts the code of version 4p1 of the Modular Ocean Model (Griffies, 2009), with 50 vertical levels and a nominal 1° horizontal resolution, refined meridionally to 1/3° near the equator (Gnanadesikan et al., 2006). The land component is Land Model, version 3, which includes five dynamically competing vegetation types (Shevliakova et al., 2009). The sea-ice component is similar to that of the model simulation in CM 2.1 (Winton, 2000).

To assess and verify model performance related to the interannual salinity variability and related physics, a model simulation is selected from the pre-industrial control experiment with a period of 30 years to match the period of the observational and reanalysis data. The model output fields include monthly ocean temperature and salinity, precipitation, evaporation, and 3D ocean currents.

2.3. *Salinity budget*

To understand the MLS variations, we investigate the factors that balance the MLS budget in the tropical Pacific. This approach has been widely used in determining the controlling processes related to salinity in order to study the MLS tendency (e.g., Zhang et al., 2006; Yu, 2011; Hasson et al., 2013; Da-Allada et al., 2014; Gao et al., 2014). This study adopts the same budget analysis method as Zhang et al. (2006), in which the equation governing MLS tendency ($\partial S'/\partial t$) can be symbolically written as

$$\begin{aligned}\frac{\partial S'}{\partial t} = {} & \underbrace{-u'\frac{\partial \bar{S}}{\partial x} - (\bar{u}+u')\frac{\partial S'}{\partial x} - v'\frac{\partial \bar{S}}{\partial y} - (\bar{v}+v')\frac{\partial S'}{\partial y}}_{A} + \underbrace{\frac{K_h}{H}\nabla_h(H\nabla_h S')}_{B} - \\ & \underbrace{[(\bar{w}+w')M(-\bar{w}-w') - \bar{w}M(-\bar{w})]\frac{(\bar{S}_e-\bar{S})}{H} - (\bar{w}+w')M(-\bar{w}-w')\frac{(S'_e-S')}{H}}_{C} + \\ & \underbrace{\frac{2k_v}{H(H+H_2)}(S'_e-S')}_{D} + \underbrace{\frac{1}{H}[(\bar{E}-\bar{P})S' + (E'-P')\bar{S} + (E'-P')S']}_{E}. \end{aligned} \tag{1}$$

Here, the subscript e represents the base of the mixed layer; S' and S'_e are anomalies of MLS and salinity at the base of the mixed layer; $\bar{S}$ and $\bar{S}_e$ refer to the climatological fields of MLS and salinity at the base of the surface mixed layer, which are specified as seasonally varying from the World Ocean Atlas 2001; $(H + H_2)$ is a constant (125 m), where H denotes the depth of the mixed layer; $M(x)$ is the Heaviside step function; u and v are the zonal and meridional components of the hori zontal ocean currents; w is the vertical velocity at the base of the mixed layer; K_v and K_h are the vertical and horizontal mixing coefficients for MLS (the vertical mixing coefficient is 1.0×10^{-7} m^2 s^{-1}, the horizontal coefficient for the zonal component of diffusion is 2.5×10^4 m^2 s^{-1}, and that for the meridional component of diffusion is

2.5×10^3 m^2 s^{-1}); E and P are evaporation and precipitation, respectively. For a detailed description, readers are referred to Zhang et al. (2006). The right-hand terms of Eq. (1) can be grouped as follows: the C and D terms act as the subsurface forcing, and the E terms are the surface forcing. Note, as in Hasson et al. (2013), horizontal mixing (the B term) is added to the horizontal advection (the A term) in order to group all horizontal processes.

2.4. *Cyclostationary empirical orthogonal function analysis*

In order to extract the modes of the principal SST anomaly and the related variability responding to SST interannual anomalies, cyclostationary empirical orthogonal function (CSEOF) analysis is applied to the SST and other oceanic anomaly fields [see Kim et al. (1996) and Kim and North (1997) for a detailed description]. In this method, the long-term monthly spatiotemporal data, of which the means are defined as $T(\hat{r},t)$, are decomposed using the following equation:

$$T(\hat{r},t) = \Sigma \mathrm{PC}_i(t)\,\mathrm{LV}_i(\hat{r}+d)\ . \tag{2}$$

Here, the subscript index i is the mode number, while r and t denote space and time, respectively $\mathrm{LV}_i(\hat{r})$ refers to the patterns of specific spatial loading vectors (LVs) and $\mathrm{PC}_i(t)$ is the corresponding principal component time series; d represents the nested period. CSEOF LVs represent time-independent patterns and periods of variability in the dataset and are often interpreted as the physical modes of the system and are derived from a time-dependent and periodic covariance function.

The most distinctive characteristic of the CSEOF technique, when compared to other traditional eigenvector analyses, is that each CSEOF LV depicts the temporal evolution related to an inherent physical process in a given dataset. The critical motivation for the time dependence of LVs is that the spatial patterns of many known phenomena in climatology and geophysics evolve temporally with well-defined periods in addition to stochastic undulations at longer time scales. Thus, typical responses of a physical system often move and change in forms instead of being stationary. It is well known that SST in the tropical Pacific undergoes a systematic change during El Niño. Since various physical processes coexist in a dataset, the nested period should be determined such that all the distinct periods of physical processes are covered. For the focus on ENSO in this study, the nested period is set to two years; this decision is based on the biennial tendency of ENSO, and a previous study has provided a reasonable physical explanation for tropical Pacific SST variability with a two-year nested period described (Kim, 2002).

3. Results

3.1. *Salinity climatological and interannual variability*

The MLS climatological mean and interannual variability simulated by GFDL-ESM2M are compared with observations. The observed climatological mean MLS distribution in the tropical Pacific is characterized by a relative maximum centered at the subtropical gyre centers in the Southern Hemisphere, where the maximum MLS is higher than 36.5 psu (Fig. 1a). The lowest MLS values (< 33 psu) are found in the narrow belt between 5°N and 10°N along the north branch of the ITCZ, and roughly in the SPCZ. Especially in the western equatorial Pacific, the region with such low salinity has been defined as the western Pacific Fresh Pool (Delcroix and Picaut, 1998). Note that the pattern of observed MLS variability is not related to that of the MLS climatological mean. As showed in Fig. 1d, the maximum MLS variabilities are found over the central-western equatorial Pacific and the Pacific coasts of Central America. Besides, its distribution of high-value regions is similar to that of tropical precipitation, such as in the ITCZ. In other words, it is evident that the interannual freshwater flux variability is the main factor affecting salinity change in the tropical Pacific, as described in Hasson et al. (2013). Consequently, as for the distribution of the observed MLS variability in tropical Pacific, the MLS variability has been shown to have negative spatial correlation with the distribution of mean MLS ($R = -0.73$). For example, the highest MLS variability occurs in the ITCZ and Fresh Pool, while a low mean MLS is located there. The observed MLS variability demonstrates that MLS changes at the interannual time scale have been shown to be chiefly due to ENSO and are located in the warm pool and SPCZ regions as well as near the equatorial American coast (Delcroix and Picaut, 1998).

Generally, GFDL-ESM2M simulates the features of the observed climatological mean and interannual variability of MLS, with several differences between the model and observations in some regions. The mean distribution of the simulated MLS in the equatorial Pacific is illustrated by three relative maxima, located at the southern subtropical gyre centers, the central equatorial Pacific and the subtropical regions of the Northern Hemisphere (Fig. 1b). Thus, compared with observations, a large positive model–observation difference appears in the equatorial Pacific, especially in the ITCZ and SPCZ. The maximum model–observation difference, located in the eastern Pacific, is as high as 2.5 psu (Fig. 1c). The large model–observation biases of MLS along the equator are linked with the model–observation difference of freshwater flux associated with the ITCZ, which is the main reason for the biases in salinity simulated in the tropical Pacific, as described by previous studies (e.g., Forget et al., 2015). For example, high salinity biases mainly occur in the SPCZ of the southern Pacific, where the simulated salinity is 0.5 to 1.5 psu lower than the observed salinity; in the subtropical Northern Hemisphere, the simulated MLS is approximately 0–0.5 psu saltier than observed.

In both the observation and simulation, the maximal interannual variabilities occur in the ITCZ and SPCZ, particularly in the western and eastern equatorial Pacific (Figs. 1d and e); this pattern is the same as that revealed by in-depth studies of observed salinity distribution (e.g., Delcroix et al., 2011). While the climatological MLS simulated by GFDL-ESM2M is lower than its observed counterpart in the Southern Hemisphere, the simulated centers of large MLS variability are

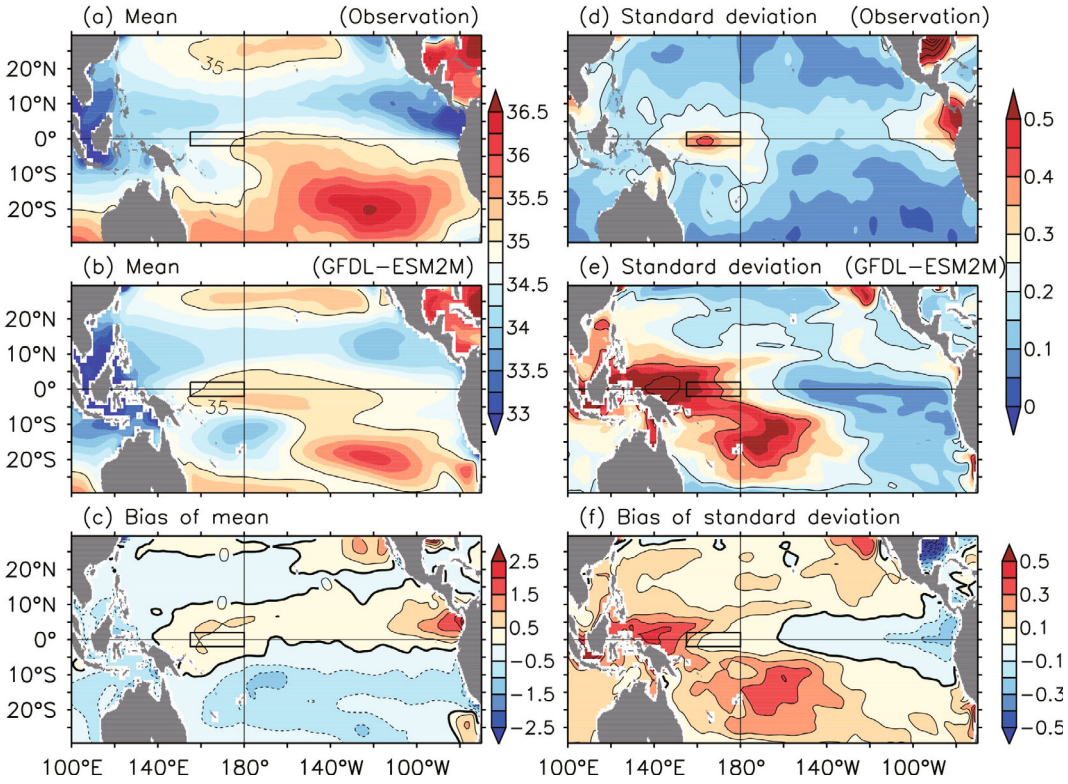

Fig. 1. (a) Observed and (b) GFDL-ESM2M-simulated climatological-mean sea surface salinity and (c) their difference (simulation minus observation), and (d) observed and (e) GFDL-ESM2M-simulated standard deviations of MLS and (f) their differences, in the tropical Pacific. The box is the so-called warm pool (2°S–2°N, 160°–180°E) region, as defined in Figs. 2 and 3. Units: psu.

mainly located in the warm pool and SPCZ, and the extent and magnitude of high interannual variability are larger than those observed (Fig. 1f).

3.2. *Salinity budget*

Following the aforementioned budget method, the determinants of the MLS tendency are defined as surface forcing, surface advection, and subsurface factors, in Eq. (1). Note that in the different regions, such as the warm pool and SPCZ, the contribution of each salinity budget term to the tendency shows distinct features (Gouriou and Delcroix, 2002). Figure 2 shows the standard deviation of the MLS tendency and budget terms along a wide tropical belt (30°S–30°N, 100°E–80°W) in the Pacific. The maximum MLS tendency ($> 20.0 \times 10^{-8}$ psu s^{-1}) occurs between approximately 10°S and 17°N west of the dateline in the equatorial Pacific and in the eastern equatorial Pacific near America, but relatively weak variabilities ($8.0–16.0 \times 10^{-8}$ psu s^{-1}) exist in a narrow band in the central equatorial Pacific and SPCZ regions (Fig. 2a). However, the MLS tendency variability in the central-western equatorial Pacific (10°S–10°N, 160°E–160°W) is primarily controlled by horizontal advection (Fig. 2b). Similarly, horizontal advection is a primary contributor to strong MLS interannual variability near America in the equatorial Pacific, as is subsurface forcing (Fig. 2c). Consistent with previous conclusions (Hasson et al., 2013), the spatial correlation (see Table 1) elucidates that the overall spatial

Table 1. Spatial correlation between MLS variability and MLS budget terms averaged in a box (2°S–2°N, 160°E–180°W) in the equatorial Pacific.

		Surface advection	Subsurface forcing	Surface forcing
MLS variability	Observation	0.41	0.31	0.67
	Simulation	0.43	0.29	0.61

pattern of the MLS variability over the box (2°S–2°N, 160°E–180°W) in the equatorial Pacific has a positive correlation with surface forcing ($R = 0.67$), whose value is followed by that of surface advection ($R = 0.41$). This implies that surface forcing and surface advection are important processes in balancing the MLS budget, but subsurface processes are not negligible. The imbalances of the surface forcing and surface advection processes are compensated by subsurface forcing by ocean vertical mixing and entrainment, including wind-induced Ekman transport (Gao et al., 2014).

Furthermore, the most important region for salinity budget terms is located near the eastern edge of the warm pool (2°S–2°N, 160°E–180°W) (i.e., the oceanic convergence zone), where maximum salinity interannual variability is found in relation to ENSO events (Maes et al., 2006). Also, the aforementioned MLS variability shows zonal displacements due chiefly to the horizontal advection of low-salinity

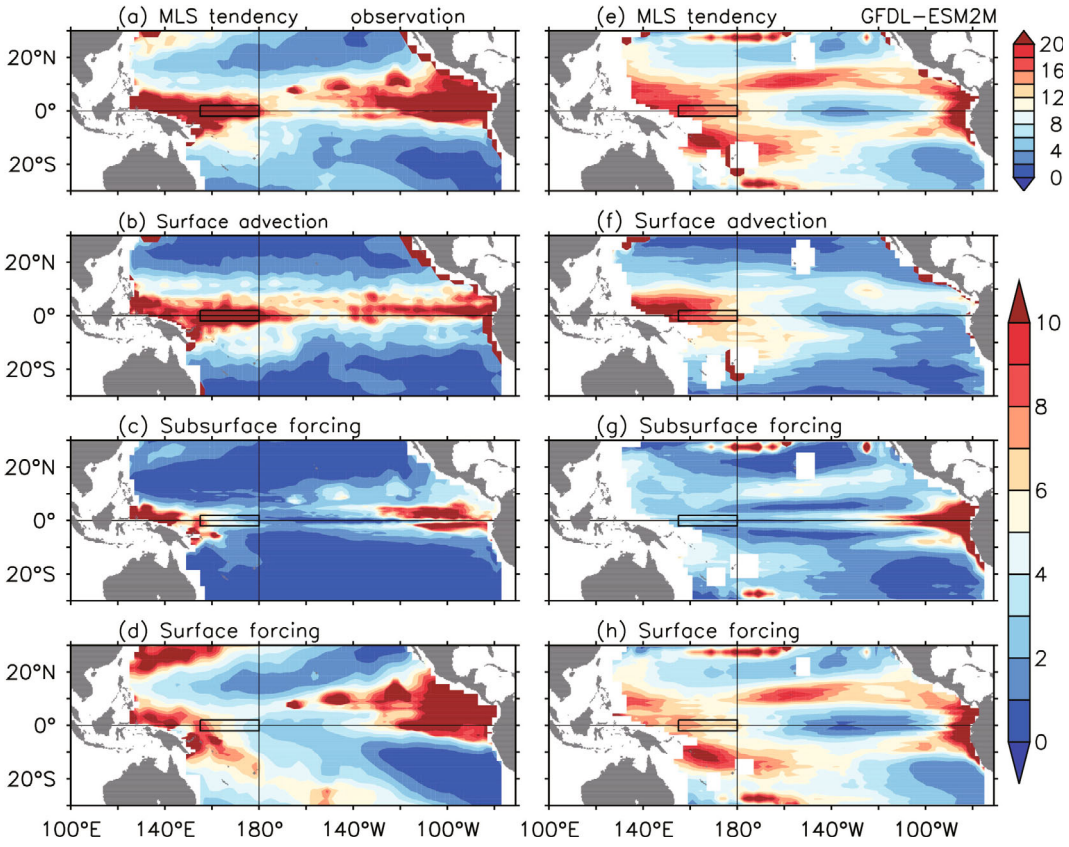

Fig. 2. Standard deviation of the (a–d) observed and (e–h) GFDL-ESM2M-simulated MLS budget terms over the tropical Pacific: (a, e) MLS tendency, and its (b, f) surface advection, (c, g) subsurface forcing, and (d, h) surface forcing budget terms. Units: 10^{-8} psu s^{-1}.

waters from the western to the central-eastern basin during El Niño (and vice versa during La Niña). The conventional salinity budget theory, therefore, assumes that the salinity tendency results from the balance between cool/warm water mass transport and ocean–atmosphere interplay associated with freshwater flux in the warm pool (Picaut et al., 1996, 2001; Vialard et al., 2002). In the tropical convergence zones, it is found that the contribution of surface forcing is strong, matching well with the equatorward advection of the freshwater belt (Fig. 2d). Compared with the subsurface forcing in the SPCZ and especially in the southern Pacific, the surface forcing also makes a large contribution to the MLS tendency, for there is plenty of precipitation. The pattern of the subsurface process agrees with Fig. 4 in Hasson et al. (2013). In particular, in the western boundary of the tropical Pacific, the contribution of the subsurface process is as critical as that of surface advection (Fig. 2c). The subsurface forcing could modulate other contributors and suppress the MLS tendency in the southwestern tropical Pacific. It is noted that the MLS variation is relatively strong in the central-eastern equatorial Pacific (160°–120°W), because large surface advection counteracts the contribution of subsurface forcing north of the equator. In contrast to the large surface forcing, the surface advection and subsurface forcing are relatively weak in the ITCZ; plus, due to the large amount of precipitation, surface forcing is the main contributor to the salinity tendency compared with subsurface forcing and surface advection in the SPCZ (Fig. 2d). On the contrary, in the subtropical gyres of both hemispheres, small values result from the weak freshwater flux in these locations (Durack et al., 2012).

The MLS tendency simulated by GFDL-ESM2M generally captures the observed characteristics of the large salinity variations in the western Pacific. However, the magnitude is weaker than its observed counterpart, particularly between 160°W and 100°W around the central-eastern equator Pacific (Fig. 2e). Similar to observation, variations of the surface forcing, horizontal advection and subsurface forcing all contribute to the interannual variations of the MLS simulated by the model (Figs. 2f–h). However, the simulated MLS budget terms show some differences with the observed budget terms. The simulated large MLS tendency ($> 8.0 \times 10^{-8}$ psu s^{-1}) associated with surface advection is located west of the dateline, while the simulated large MLS tendency linked to subsurface forcing only exists in the eastern tropical Pacific. Surface forcing makes great contributions in both the southern and northern tropical Pacific, with the largest contributions located in the SPCZ and near South America

In contrast to the observed spatial displacements, the simulated surface forcing dominates the MLS tendency. A large interannual variability is observed in the area west of the dateline in the western-central equatorial Pacific, while the simulated large variabilities mainly occur in the ITCZ,

SPCZ and warm pool. Moreover, comparison among the influences of MLS budget terms on MLS variability shows that the MLS tendency primarily arises from surface forcing in the equatorial Pacific, followed by surface advection (Table 1). The discrepancies between observation and simulation are caused by the differences between simulated and observed ocean physics. For example, the simulated freshwater flux is larger than observed in the warm pool, SPCZ and ITCZ, but weaker than observed in the central-eastern region (Figs. 3a, d and g); the simulated ocean zonal current is significantly weaker than observed in the equatorial Pacific, especially in the central-eastern equatorial Pacific (Figs. 3b, e and h); and the simulated vertical velocity is generally weaker than observed in the tropical Pacific, especially in the central-western equatorial Pacific (Figs. 3c, f and i). Despite the simulated weaker surface advection caused by the simulated weaker ocean circulation, its relationship with MLS tendency is higher than in observations. In contrast, due to the large amounts of precipitation in the interannual variations of freshwater flux, the surface forcing components indicate that the freshwater flux component dominates the total salinity budget in the warm pool and SPCZ. The effect of surface forcing on the MLS variability in the eastern equatorial region is closely associated with the distribution of salinity variability. Meanwhile, the subsurface processes provide evident effects along the equator, mainly because of the obvious upwelling and the large vertical salinity gradient in this region (Gao et al., 2014). However, simulated weak vertical velocity leads to a smaller effect of subsurface forcing than observed in the central-eastern equatorial Pacific.

3.3. *Evolution of interannual salinity variability and its budget in the mixed layer*

The simulation by GFDL-ESM2M is further assessed in terms of the evolution of MLS and the interannual variability of related physics, including the SSTA and corresponding anomaly term of the MLS budget. Figures 4 and 5 compare the observed and simulated MLS time series averaged over a 4° latitude by 20° longitude region where large MLS variability exists; the region is in the warm pool (2°S–2°N, 160°–180°E). The box is selected based on the criteria described in Hasson et al. (2013). Compared to the evolution of Niño3.4 index and each MLS budget term, the two time series illustrate the signature of interannual variations with a clear tendency for MLS (Fig. 4a). At interannual scales, the domain-averaged MLS tendency fluctuates within $\pm 4.0 \times 10^{-8}$ psu s^{-1}. The fluctuation of MLS tendency exhibits an approximate period of four to seven years. Because the observed relationship between the interannual evolutions of MLS tendency in the warm pool and Niño3.4 index is −0.73, the evolution of MLS tendency in the warm pool is closely related to ENSO in the observations.

Further inspection of individual budget terms in the warm pool indicates that surface advection and surface forcing are important components (which have the same orders of magnitude but with opposite signs), and the contribution of subsur-

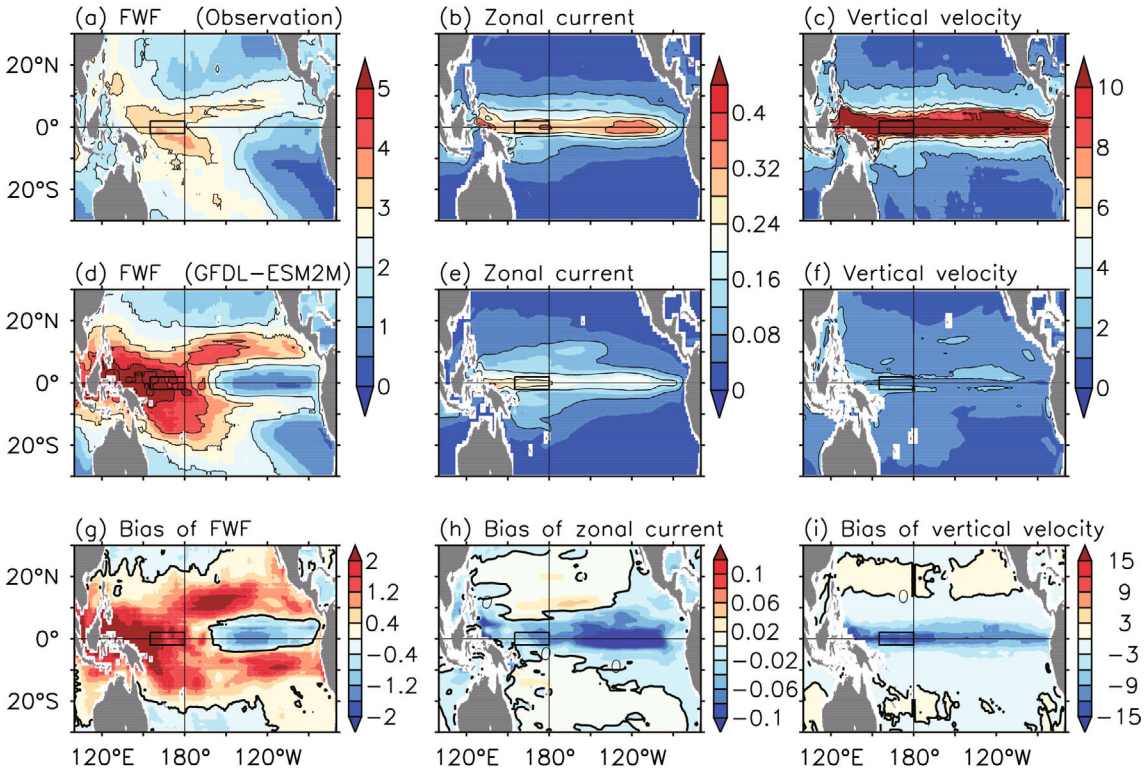

Fig. 3. Standard deviations of (a, d, g) freshwater flux (units: 10^{-6} mm s^{-1}), (b, e, h) zonal current (units: m s^{-1}), and (c, f, i) vertical velocity (units: 10^{-6} m s^{-1}) at the base of the mixed layer: (a–c) observed; (d–f) simulated by GFDL-ESM2M; (g–i) differences between observation and simulation.

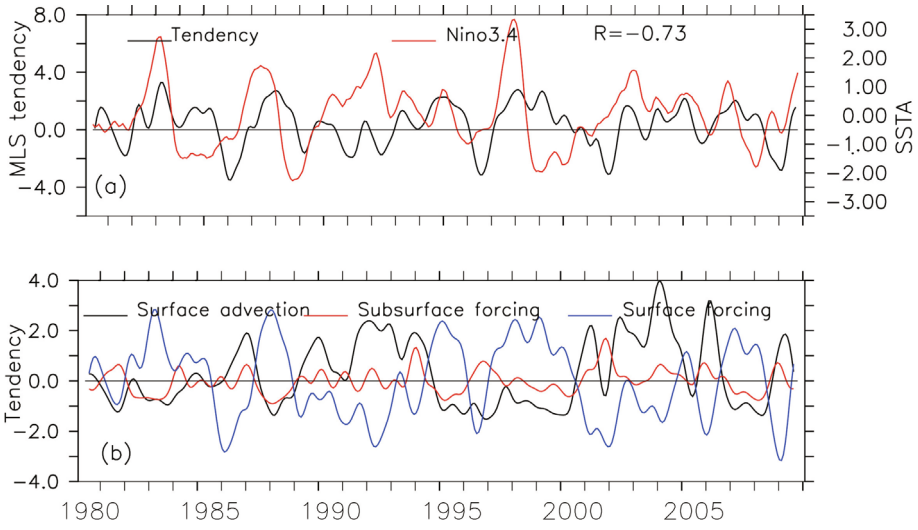

Fig. 4. Time series of interannual variations observed during 1980–2010 for the (a) region-averaged MLS tendency and Niño3.4, and (b) region-averaged MLS budget terms in the warm pool (2°S–2°N, 160°–180°E), including surface advection, subsurface forcing and surface forcing. *R* is the correlation coefficient between the MLS tendency mean in the warm pool and Niño3.4 as indicated in Fig.6. Units: 10^{-8} psu s^{-1} for MLS tendency and its budget terms, and °C for SSTA.

face forcing is relatively small (Fig. 4b). In particular, with the positive and negative anomalies of Niño3.4 index, subsurface forcing makes a weak contribution to the tendency of MLS. Generally speaking, variations in the interannual MLS tendency are captured by the summed contributions of MLS budget terms, including the air–sea forcing, oceanic advection, diffusion, and entrainment in the warm pool (Figs. 4a and b). In the temporal evolutions of salinity budget terms, MLS tendency is mainly controlled by surface forcing, followed by surface advection and subsurface forcing. The latter two terms of MLS tendency compensate for the effect of surface forcing on it. The MLS tendency is closely associated with the surface forcing term, with the maximum negative/positive peak during La Niña and El Niño events in the warm pool. The negative/positive surface forcing corresponds to positive/negative Niño3.4 index (i.e., El Niño/La Niña). Similar relationships in the warm pool at interannual scales were also obtained by the studies of Hasson et al. (2013) and Gao et al. (2014), who deduced that the interannual variability of vertical entrainment is relatively weak in the tropical Pacific in contrast to other budget terms.

GFDL-ESM2M captures the features of the interannual variation in MLS tendency by the sum of MLS budget terms. The simulated tendency of MLS presents significant interannual oscillation, and its simulated positive/negative peak is within the range of 5.8 to -6.0×10^{-8} psu s^{-1} compared to the observed range of 3.9 to -3.8×10^{-8} psu s^{-1}. Similar to the observed relationship between the interannual evolutions of MLS tendency mean in the warm pool and Niño3.4 index, the simulated relationship is −0.76 higher than in the observation (Fig. 5a). It is shown that the simulation also captures the observed lag/lead relationship between the MLS tendency and Niño3.4 as well as the compensation for surface advection and subsurface forcing of the salinity budget terms (Fig. 5b). The weaker simulated subsurface forcing and surface advection lead to a weaker compensation effect on the interannual variation of MLS, and the model exaggerates surface forcing in the salinity budget, inducing larger MLS variability than in the observation. So, the simulated salinity tendency depends more on the interannual change in freshwater flux. Meanwhile, the weaker compensation effect on the salinity tendency from surface advection and subsurface forcing mainly results from weaker simulated ocean currents.

As shown in Fig. 6, there is a close relationship between Niño3.4 index and MLS tendency in both the observation and simulation, especially when the MLS tendency leads the Nino3.4 index by about 12 months, with the most significant correlation coefficient being −0.78. This lead/lag relationship is clearly seen in the 1982/83, 1988/89, 1997/98 El Niño events. The aforementioned relationship suggests that the MLS tendency has the potential to be used as a predictor of ENSO. The model can represent the lead/lag relationship between Niño3.4 index and MLS tendency, but the most significant lead time is 8–10 months, which is shorter than that in the observation.

3.4. *Evolution of MLS and its budget during ENSO cycles*

This subsection focuses on the differences in the MLS budget in the equatorial Pacific by comparing observed ENSO (cool/warm) events to those simulated by GFDL-ESM2M. We use CSEOF analysis to calculate the dominant modes of SST variability over the tropical Pacific (30°S–30°N, 100°–230°E) over a 30-year period. Because the nested period is set to two years, each CSEOF LV depicts the SST anomaly spatial evolution during 24 months related to an inherent physical process in a given dataset. For brevity,

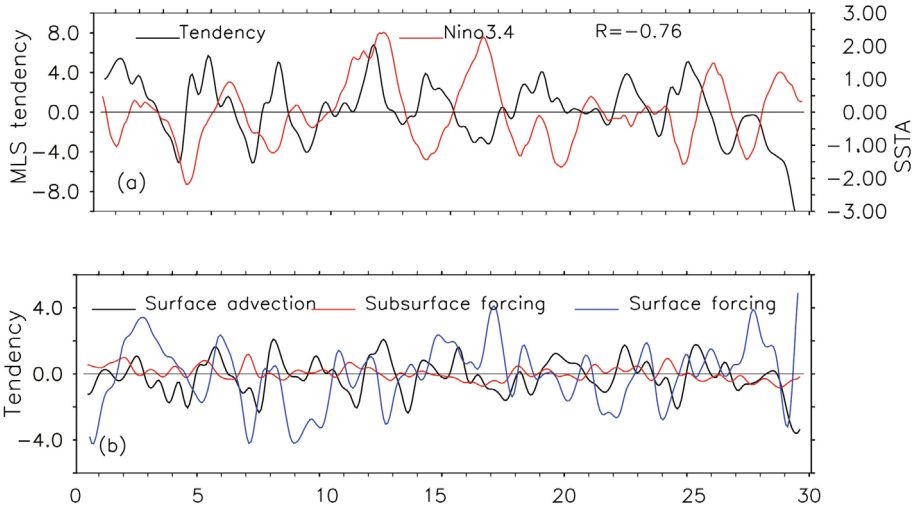

Fig. 5. As in Fig. 4 but for GFDL-ESM2M during the last 30 years in pre-industrial control experiment.

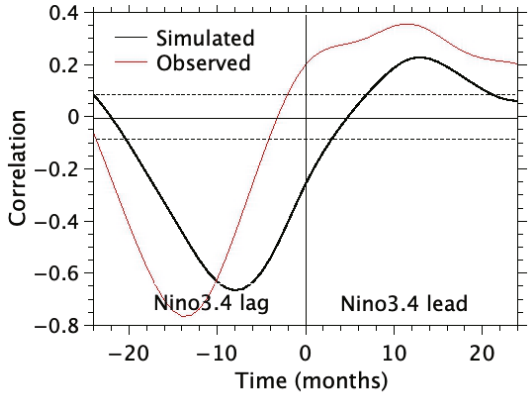

Fig. 6. Lead/lag correlations between Niño3.4 and the warm pool MLS tendency. The red line is for observations during 1981–2100 and the black line is for the GFDL-ESM2M simulation during the last 30 years of pre-industrial control run. The dotted lines represent the 95% confidence level.

the three-month averaged SSTA and the corresponding MLS anomaly and its budget terms are presented in the ENSO cycle.

3.4.1. *MLS*

Given these CSEOF characteristics, the MLS and each budget term's anomalies regressed with the principal component (PC) 1 of the SSTA from CSEOF are used to better discriminate between the cool/warm phases of ENSO. Figure 7a shows the first mode LV of the CSEOF SSTA (left) and the corresponding observed MLS (right) regressed to PC1. Here, the first CSEOF mode LV represents approximately 42% of the total variance compared with the second CSEOF mode LV, which represents approximately 21% of the total variance. As for the LV of the first CSEOF modes, the evolution of its spatial patterns exhibits a distinct oscillation within the nested period (Fig. 7a), which represents biennial oscillations of SSTAs in the tropical Pacific (Kim, 2002). Figure 7b shows the PC time series of the first CSEOF LV mode and Niño3.4 index; the correlation coefficient between these two time series reaches 0.82. The SSTA evolution and its regressed MLS patterns of the first SSTA CSEOF LV portray the development of El Niño and La Niña events and show details of the phase transitions between El Niño and La Niña. In addition to the oscillatory nature of the first CSEOF mode, its feature demonstrates that this mode fits the description of canonical ENSO (Kug and Kang, 2006; Yoo et al., 2010; Kim et al., 2011, Yeo and Kim, 2014), with the intensity of SST change confined to a narrow equatorial zone, while the SSTA in the northern North Pacific is relatively weak.

As shown in Fig. 7a, during April to June of year 1, a warm SSTA in the eastern tropical Pacific occurs and develops, then moves towards the central tropical Pacific in successive months during July to September of year 1, and reaches its maximum amplitude in October December of the same year. Corresponding to the spatial evolution of the SSTA, the positive MLS anomaly in the western Pacific begins to weaken gradually, and turns into the negative MLS anomaly westward across the dateline in the eastern-central Pacific. During October to December of year 1, which is defined as the peak phase of El Niño, the maximum negative MLS anomaly (< -0.3) moves near the dateline along the equator, and the SPCZ region is marked by high-salinity anomalies. The MLS distribution presents a feature whereby negative MLS anomalies are zonally distributed along the equator (maximum of 0.3) and positive MLS lies mainly outside the equatorial Pacific: one is centered west of the dateline between 10°N and 20°N (maximum of 0.29) and the other appears approximately between 30°S and 20°S (maximum of 0.21). After El Niño reaches the mature stage in January March of year 2, the positive and negative MLS anomalies reach their maximum amplitude. From April to June of year 2, the SSTA mode begins to change to the cold phase, and positive MLS anomalies in the south and north subtropical regions, especially in the SPCZ and ITCZ, retract towards the equator. The corresponding La Niña matures during October

to December of year 2, and a positive MLS anomaly occupies the tropical western Pacific and extends across the dateline. As shown in the MLS during the ENSO cycle, the displacements of the regressed MLS anomaly are somewhat asymmetric in the equatorial Pacific compared to La Niña and El Niño. So, the advantage of using this SSTA CSEOF method is that it can present a concise description of the spatiotemporal evolution of the SSTA and corresponding MLS anomaly

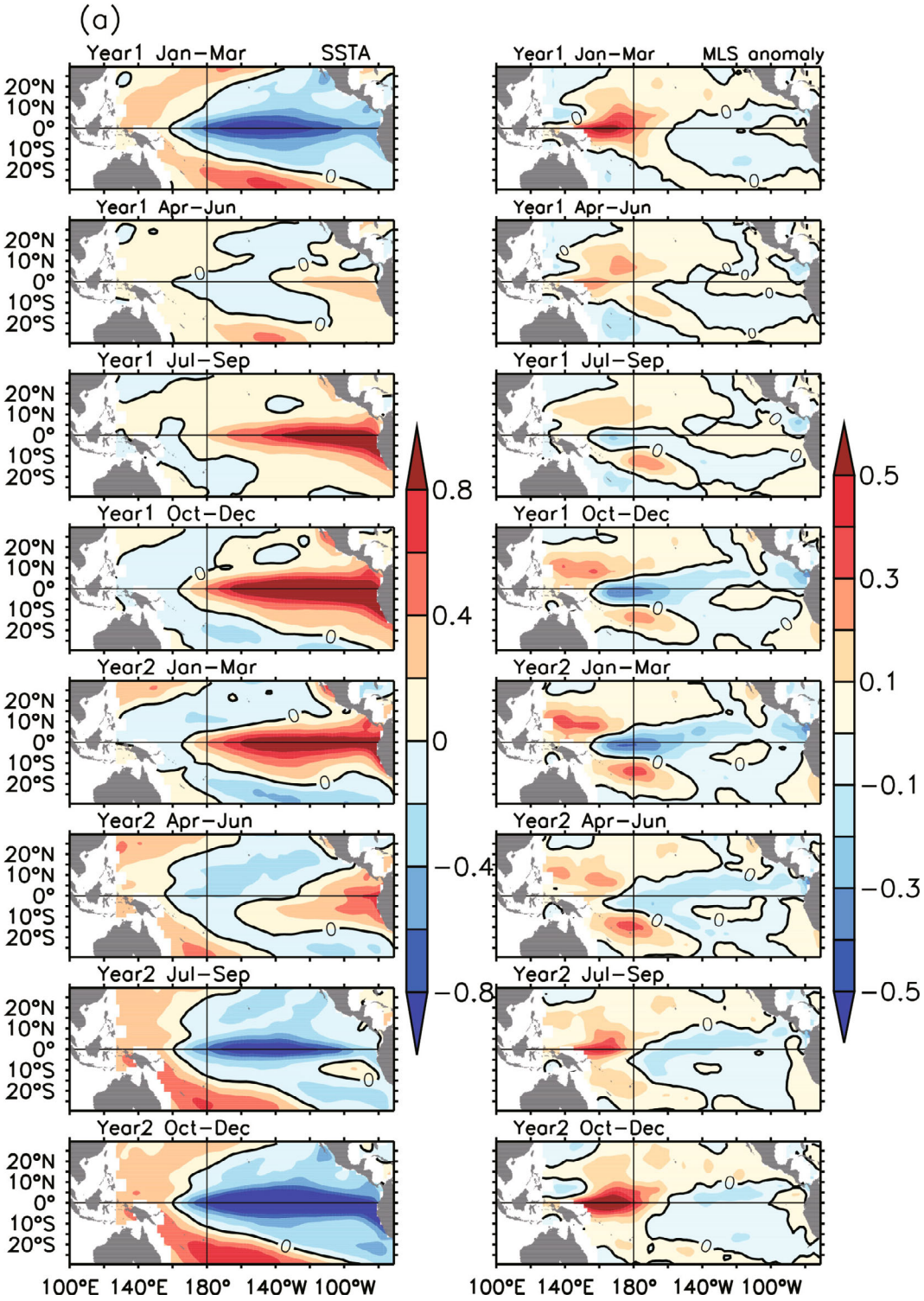

Fig. 7. (a) The observed first CSEOF LVs of SSTA and the regressed MLS anomalies to the CSEOF PC1 of the SSTA via three-month averaging. The presented patterns illustrate the evolution of the CSEOF LV averaged from January of year 1 to December of year 2, representing the spatial pattern from La Niña to El Niño. (b) The PC time series (eigenvalues) of the first CSEOF mode and Niño3.4 index. Units: °C for SSTA, and psu $(°C)^{-1}$ for the regressed MLS.

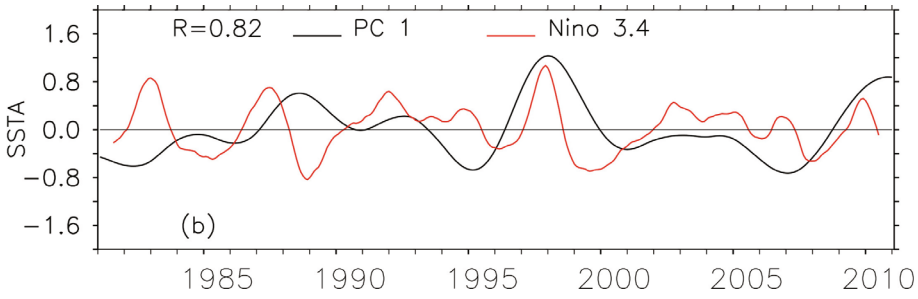

Fig. 7. (Continued)

during ENSO.

As for the LV of the CSEOF simulated by GFDL-ESM2M, the spatial pattern of the first CSEOF mode exhibits no notable change within the nested period (not shown), which explains approximately 37% of the total variance in the SST field. Thus, this mode can be considered to be nearly stationary. The SSTA first CSEOF LV pattern in the tropical region is broader in the meridional direction than in the conventional ENSO signal, and positive anomalies extend from the northeastern to southeastern midlatitude Pacific. Also, it presents strong SSTAs in the tropical central Pacific, which corresponds to the typical features observed during CP-type El Niño events (CP: central Pacific). Then, the second mode represents the biennial oscillations of the SSTA (Fig. 8a). PC2 explains approximately 17% of the total variance in the simulated data, and the temporal correlation coefficient with Niño3.4 index is 0.91 (Fig. 8b), which demonstrates that the second SSTA CSEOF LV and corresponding regressed MLS anomaly can capture the observed features of the El Niño and La Niña cycle. Compared with observations, amplifications of the positive and negative anomalies simulated by the model, which represent ENSO-induced cool/warm cycles, are stronger and extend farther westward. The biases may be caused by the greater SST interannual variability than its observed counterpart in the tropical Pacific. On the other hand, the regressed MLS LV in the warm pool that corresponds to the ENSO cycle reproduces the shift from the positive to negative anomaly as in the observations, and the salinity anomaly is stronger during El Niño but weaker and farther to the west during La Niña than in the observations. In particular, during both El Niño and La Niña, the simulated positive MLS anomaly occurs east of the SPCZ in the southern tropical Pacific, while the negative MLS anomaly is located in the northeastern tropical Pacific. Perhaps the positive anomalies are not very significant compared to the MLS variability in the other regions of the tropical Pacific, as they seem to occur in a region of low variability. This difference might be associated with the biases in the simulated spatial distribution of interannual variability.

3.4.2. *MLS budget*

The regressed spatial patterns of budget terms explain the spatial evolution of MLS variability during the ENSO cycle. Figure 9 shows the regressed terms of the MLS budget observed by the PC1 of CSEOF SSTA. The spatial pattern in January to March of year 1 shows high negative anomalies for the surface advection term [a minimum of -4.0×10^{-8} psu s^{-1} $(°C)^{-1}$], which is seen mostly across the equatorial Pacific, and a large negative anomaly for the subsurface forcing term is located west of the dateline. In contrast, a stronger positive surface forcing anomaly [more than 5.0×10^{-8} psu s^{-1} $(°C)^{-1}$] is located at the mean ITCZ position, while the SST corresponds to the termination of La Niña in April to June of year 1. Meanwhile, the negative surface advection anomaly begins to weaken and shrink to the west, whereas the weak negative anomaly for subsurface forcing in the western-central equatorial Pacific becomes positive, and the positive surface forcing anomaly in the equatorial Pacific fades and becomes a negative one, which corresponds to the zone of rainfall changes at the equator. During the mature El Niño period of January to March of year 2, an area of negative surface forcing anomaly extends westward along the equator across the dateline, and the negative maximum anomaly appears near the dateline; a positive anomaly for subsurface forcing forms in the western-central equatorial Pacific, with the maximum center being located to the west of the dateline. Corresponding to the development of precipitation in the ITCZ during El Niño, a negative anomaly for surface forcing moves westward and governs the position of the ITCZ. During April to June of year 2, corresponding to the decay of El Niño, the positive anomaly for surface advection begins to decrease and shrink to the east along the equator, while the positive anomaly of subsurface forcing weakens and becomes negative. The surface forcing anomaly moves eastward, and the negative surface forcing anomaly returns to the western equatorial Pacific, while a positive one is found over the ITCZ region. Finally, corresponding to the mature La Niña during October to December of year 2, large anomalies for the salinity budget terms are seen in the tropical Pacific, while negative anomalies for surface advection and subsurface forcing are located in the western-central equatorial Pacific, which correspond to the positive surface forcing anomalies that are governed by the position of the ITCZ.

Figure 10 shows the regressed terms of the MLS budget simulated by the PC2 of CSEOF SSTA. During the evolution of ENSO, salinity budget terms simulated by GFDL-ESM2M exhibit several biases in distribution and magnitude of variables compared to the observed. As shown, the anomaly of the three terms moves back and forth across the dateline along the equator from January to March of year 1 to October to

December of year 2, which lead to an MLS anomaly in the equatorial Pacific during ENSO. For example, from January to March of year 1 to October to December of year 1, the surface advection changes from a negative anomaly to a positive anomaly in the warm pool. It then changes to a negative anomaly during October to December of year 2. The corresponding surface forcing near the dateline also changes from positive to negative and then back to positive. Because of the weak simulated interannual variability of the vertical velocity in the equatorial Pacific, it is not obvious that changes in subsurface forcing show weak positive anomalies during La Niña and negative anomalies during El Niño. The spatial

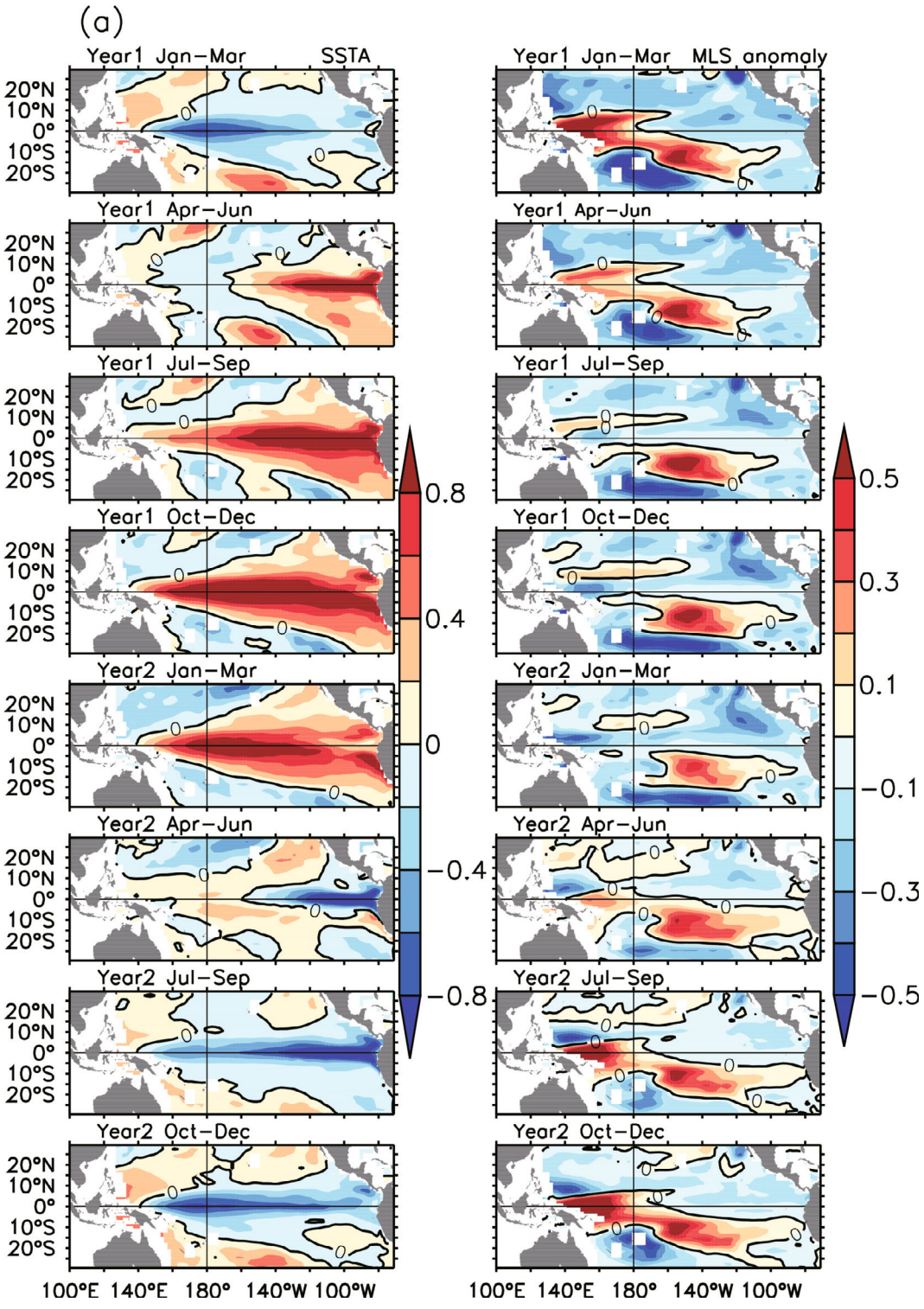

Fig. 8. As in Fig. 7 but for the second CSEOF LVs of the SSTA and regressed MLS anomalies to the CSEOF PC2 simulated by GFDL-ESM2M.

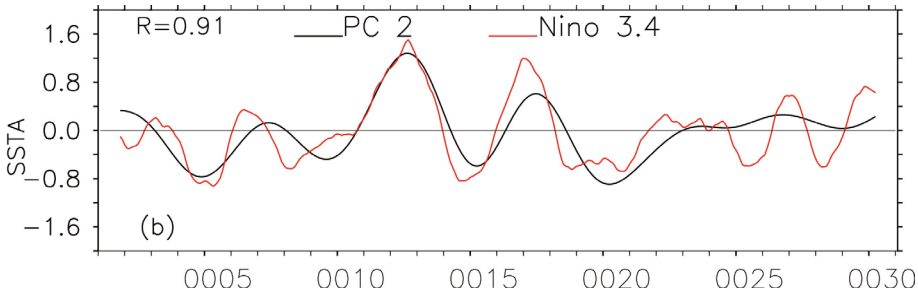

Fig. 8. (Continued)

pattern of salinity budget terms indicates that the MLS tendency is mainly controlled by the surface forcing term and has little dependence on the other terms. Compared to observations, the effect of freshwater flux variability on salinity is exaggerated. Because of the existence of the double ITCZ in simulated precipitation, the influence of freshwater flux leads to a bias in the MLS interannual variability, which ultimately affects the pattern of SST anomalies (Zhang and Busalacchi, 2009). In addition, the spatial and temporal patterns of the MLS tendency are more sensitive to precipitation in the equatorial Pacific compared to observations.

The simulated biases of MLS variability may be caused by the interannual variability in freshwater flux, which leads to biases in oceanic physics in the equatorial western Pacific and MLS displacement (Qu et al., 2013). In addition, the simulated ocean current is weaker than its observed counterpart in the equatorial Pacific (Fig. 3), which induces a weaker advection contribution to the salinity budget, including surface advection and subsurface effect. In general, based on the contribution to the MLS tendency and the relationship between SST anomaly and salinity budget terms, the simulated MLS anomaly is sensitive to the simulated oceanic physical processes associated with MLS. On the other hand, GFDL-ESM2M also demonstrates that, in the warm pool, freshwater flux related to precipitation is an important physical field for ocean salinity along the equator, and its biases affect the simulation of ocean salinity. This result confirms the significance of ocean dynamics in regulating the MLS variation during the ENSO cycle.

4. Summary and conclusion

Salinity is a prominent physical parameter in climate simulation and its spatiotemporal displacement in the equatorial Pacific is associated with temperature displacement (Delcroix and Hénin, 1991). With the development of climate models, the simulation of salinity and related physical fields has become a criterion for evaluating their performance. However, recent understanding of salinity variations and their effect on climate is still insufficient. Salinity, a primary oceanic state quantity, is more uncertain than oceanic temperature in model simulations. Hence, based on the behavior of ocean salinity from current coupled models, a detailed understanding of ocean salinity variations has been a long-standing and urgent research goal. This study used GFDL-ESM2M as an example of an Earth system model, and examined the simulated MLS spatiotemporal characteristics and the interannual variability of its budget in the tropical Pacific and the underlying cause during ENSO.

The MLS interannual variability is sensitive to the oceanic and atmospheric physics. Compared with observations, the MLS variability simulated by GFDL-ESM2M exhibits several biases in the tropical Pacific: the simulated MLS is too high in the tropical Pacific north of the equator and too low south of it; for the key regions, the simulated MLS interannual variation is generally too high, especially in the southern branch of the warm pool and ITCZ. The MLS variation can be derived from a combination of dynamic and thermodynamic processes, which depend on the intrinsic oceanic physics and forcing. The biases in representing the simulated tropical physics, including simulated horizontal and vertical ocean circulations that are weaker than observed and the problem of the double ITCZ phenomenon, lead to the biases in MLS budget terms, such as exaggerated influences of surface forcing on the MLS variation and underestimated effects of surface advection and subsurface forcing. As a result, the simulated spatial pattern of MLS tendency shows a displacement compared to observation, and such a biased spatial pattern bears a close resemblance to the spatial variation of precipitation and surface current in the equatorial Pacific.

Taking advantage of CSEOF analysis, the regressed MLS and its budget indicate that those patterns of MLS variation and related physics characterize the spatial evolution signals during the ENSO cycle according to the observed and simulated SST CSEOF LVs. The ENSO cycle that is related to the displacement of the MLS anomaly is explained by different contributions of the salinity budget terms in the equatorial Pacific. It is noted that both the observed and the simulated MLS tendency in the warm pool show a lead/lag relationship with ENSO evolution, and differences exist among the contributions of MLS budget terms to MLS tendency during ENSO. The observed results indicate that a negative/positive MLS tendency leads El Niño/La Niña by approximately 12 months. For the temporal evolutions of salinity budget terms in the warm pool, the MLS tendency is mainly controlled by surface forcing, followed by surface advection, and subsurface forcing is the smallest. Note, however, that subsurface forcing is not negligible, because subsurface forcing along with surface advection can compensate for the effect of sur-

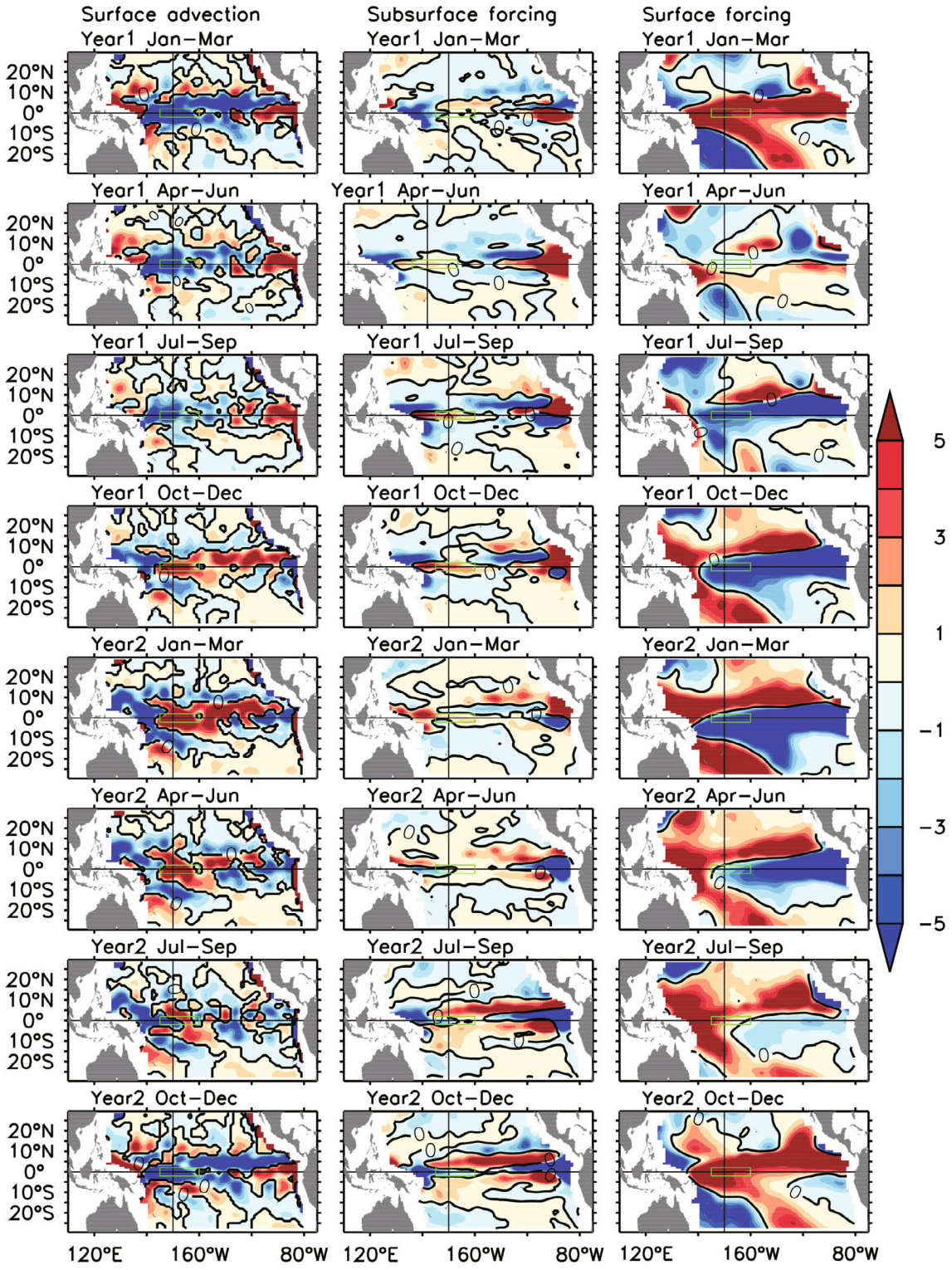

Fig. 9. Regressed MLS budget terms to the CSEOF PC1 of the observed SSTA via three-month averaging, including surface advection (left-hand panels), subsurface forcing (middle panels) and surface forcing (right-hand panels). The green boxes outline (2°S–2°N, 170°E–160°W). Units: 10^{-8} psu s^{-1} $(°C)^{-1}$.

face forcing on the MLS tendency. The model can also capture the lead/lag relationships between salinity tendency and Niño3.4 index during ENSO, despite the simulated lead time being slightly shorter than in the observation. However, due to the simulated weaker ocean currents, the simulated compensation effect of surface advection and subsurface forcing on the salinity budget term is too low, thus increasing the positive feedback of freshwater flux to MLS tendency. In addi-

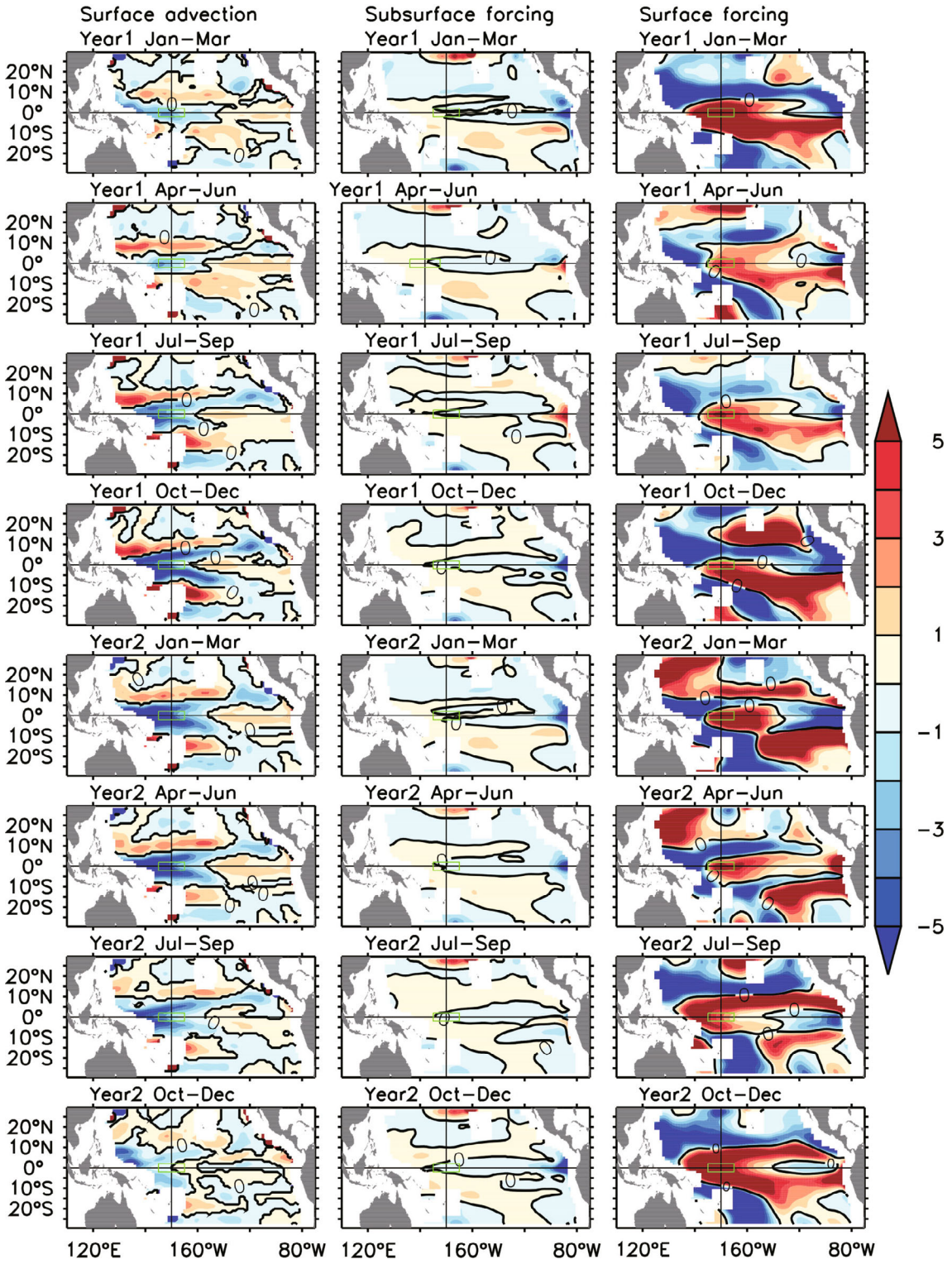

Fig. 10. As in Fig. 9 but for the regressed anomalies of the MLS budget to the CSEOF PC2 of the SSTA simulated by GFDL-ESM2M.

tion, we checked another reanalysis product and found similar results (not shown). Hence, it is evident that the simulated climate variability of the coupled model strongly depends on ocean physical processes and the ocean–atmosphere relationship represented in models, including ocean water-cycle and three-dimensional ocean circulation, as well as the vertical distribution of ocean layers.

Analyzing the relationship between SST and salinity using CSEOF is attempted in this paper, but several problems have been found. The modes of principal SST ex-

tracted by CSEOF also exhibit differences between observations and simulation. The analyses find that the first observed CSEOF LV mode is the traditional ENSO cycle (42%), whereas the second simulated CSEOF mode is the traditional ENSO (17%). This difference shows that the representation of the physical processes that affect interannual variability in the model is different from that in the observations, which leads to the weakening of explained variance of the traditional ENSO model. This actually reduces the intensity and frequency of the traditional ENSO signal. Because the CSEOF analysis requires high quality data, several simulated gridded data of physical fields in the western Pacific cannot pass the significance test, leading to default data in the spatial distribution of the LV mode. This requires us to pay attention to the quality of the data, especially the interpolated data, when using CSEOF. Secondly, the variability of analyzed fields should be matched in the selected nested period in CSEOF. In this study, for example, the regressed MLS corresponding SST CSEOF appears as a constant value in the southern Pacific during the nesting of CSEOF, due to the special period of local MLS variability, which is greater or longer than the selected nested period ($d = 24$ months).

In addition, our conclusions have several limitations. These analyses show that the different contributions from the budget terms can explain the asymmetry of the spatial evolution of MLS in some regions, including the ITCZ, warm pool and SPCZ. The warm pool is selected as a representative region to estimate the contributions of the terms to the evolution of MLS during ENSO (Delcroix and Picaut, 1998). The region has the following features: SST values warmer than 28°C–29°C; MLS values below 34.5 psu; a large MLS variability; and significant differences between the budget terms during El Niño and La Niña. Moreover, it has been found that salinity variability can contribute to climate variability by modulating SST, which may vary geographically and with time in the tropical Pacific. Such work has been done in other special regions, e.g., in the SPCZ and Fresh Pool of the tropical Pacific (e.g., Delcroix and McPhaden, 2002; Hasson et al., 2013). Secondly, this study is based on simulation from just one selected climate model (i.e., the GFDL model); the derived results might be model-dependent. Meanwhile, the salinity variability is sensitive not only to the ocean water cycle and 3D ocean circulation, but also to the vertical distribution of ocean layers. More analyses using more multi-model simulations and observation and reanalysis data are clearly needed in the future.

In general, based on the aforementioned analyses, it is found that GFDL-ESM2M, as one model of CMIP5, may exhibit several biases in simulating the MLS and related physical processes in the tropical Pacific. The simulated ocean salinity possesses certain differences compared to observations. Salinity has no direct effect on the atmosphere and the simulated salinity mainly depends on the precipitation and ocean dynamics. The simulated precipitation biases act to produce the incorrect surface salinity by the budget terms. This case generally exists because the precipitation is difficult to simulate well with atmospheric general circulation models (Lin, 2007) and even more difficult in coupled models due to the amplifying effect of air–sea interaction (Li and Xie, 2012, 2014; Ham and Kug, 2014). In the ocean model, for example, the mixing process in the upper ocean is difficult to represent accurately. This can affect the vertical distribution of salinity and temperature, which can further affect the ocean currents. Thus, the simulated biases may also exist in the ocean dynamics. The mixing processes can result in the simulated salinity biases. Additionally, Hackert et al. (2014) reported that satellite-retrieved sea surface salinity with ARGO-observed salinity data can provide better ocean analysis fields, which lead to better representations in simulating salinity. With those research efforts, salinity and the related processes will be better represented in model simulations.

Acknowledgements. The authors wish to thank the anonymous reviewers for their numerous comments that helped improve the original manuscript. This study was supported by the National Natural Science Foundation of China (Grant Nos. 41690122, 41690120 and 41475101), the NSFC–Shandong Joint Fund for Marine Science Research Centers (Grant No. U1406401), the NSFC Innovative Group Grant (Project No. 41421005), and Taishan Scholarship.

REFERENCES

Adler, R. F., and Coauthors, 2003: The version-2 global precipitation climatology project (GPCP) monthly precipitation analysis (1979–present). *Journal of Hydrometeorology*, **4**, 1147–1167, https://doi.org/10.1175/1525-7541(2003)004<1147:TVGPCP>2.0.CO;2.

Behringer, D. W., M. Ji, and A. Leetmaa, 1998: An improved coupled model for ENSO prediction and implications for ocean initialization. Part I: The ocean data assimilation system. *Mon. Wea. Rev.*, **126**, 1013–1021, https://doi.org/10.1175/1520-0493(1998)126<1013:AICMFE>2.0.CO;2.

Bingham, F. M., G. R. Foltz, and M. J. McPhaden, 2010: Seasonal cycles of surface layer salinity in the Pacific Ocean. *Ocean Science*, **6**(3), 775–787, https://doi.org/10.5194/os-6-775-2010.

Da-Allada, C. Y., F. Gaillard, and N. Kolodziejczyk, 2015: Mixed-layer salinity budget in the tropical Indian Ocean: Seasonal cycle based only on observations. *Ocean Dynamics*, **65**, 845–857, https://doi.org/10.1007/s10236-015-0837-7.

Da-Allada, C. Y., Y. du Penhoat, J. Jouanno, G. Alory, and N. M. Hounkonnou, 2014: Modeled mixed-layer salinity balance in the Gulf of Guinea: Seasonal and Interannual variability. *Ocean Dynamics*, **64**(12), 1783–1802, https://doi.org/10.1007/s10236-014-0775-9.

Delcroix, T., and C. Hénin, 1991: Seasonal and interannual variations of sea surface salinity in the tropical Pacific Ocean. *J. Geophys. Res.*, **96**(C12), 22 135–22 150, https://doi.org/10.1029/91JC02124.

Delcroix, T., and J. Picaut, 1998: Zonal displacement of the western equatorial Pacific "fresh pool". *J. Geophys. Res.*, **103**(C1), 1087–1098, https://doi.org/10.1029/97JC01912.

Delcroix, T., and M. McPhaden, 2002: Interannual sea surface salinity and temperature changes in the western Pacific warm

pool during 1992–2000. *J. Geophys. Res.*, **107**(C12), 8002, https://doi.org/10.1029/2001JC000862.

Delcroix, T., M. J. McPhaden, A. Dessier, and Y. Gouriou, 2005: Time and space scales for sea surface salinity in the tropical oceans. *Deep Sea Research Part I*: *Oceanographic Research Papers*, **52**(5), 787–813, https://doi.org/10.1016/j.dsr.2004.11.012.

Delcroix, T., G. Alory, S. Cravatte, T. Corrège, and M. J. McPhaden, 2011: A gridded sea surface salinity data set for the tropical Pacific with sample applications (1950–2008). *Deep Sea Research Part I*: *Oceanographic Research Papers*, **58**(1), 38–48, https://doi.org/10.1016/j.dsr.2010.11.002.

Dong, S. F., S. L. Garzoli, and M. Baringer, 2009: An assessment of the seasonal mixed layer salinity budget in the Southern Ocean. *J. Geophys. Res.*, **114**(C12), C12001, https://doi.org/10.1029/2008JC005258.

Dunne, J. P., and Coauthors, 2012: GFDL's ESM2 global coupled climate–carbon earth system models. Part I: Physical formulation and baseline simulation characteristics. *J. Climate*, **25**, 6646–6665, https://doi.org/10.1175/JCLI-D-11-00560.1.

Dunne, J. P., and Coauthors, 2013: GFDL's ESM2 global coupled climate–carbon earth system models. Part II: Carbon system formulation and baseline simulation characteristics. *J. Climate*, **26**(7), 2247–2267, https://doi.org/10.1175/JCLI-D-12-00150.1.

Durack, P. J., S. E. Wijffels, and R. J. Matear, 2012: Ocean salinities reveal strong global water cycle intensification during 1950 to 2000. *Science*, **336**(4080), 455–458, https://doi.org/10.1126/science.1212222.

Forget, G., J.-M. Campin, P. Heimbach, C. N. Hill, R. M. Ponte, and C. Wunsch, 2015: ECCO version 4: An integrated framework for non-linear inverse modeling and global ocean state estimation. *Geoscientific Model Development*, **8**, 3071–3104, https://doi.org/10.5194/gmd-8-3071-2015.

Gao, S., T. D. Qu, and X. W. Nie, 2014: Mixed layer salinity budget in the tropical Pacific Ocean estimated by a global GCM, *J. Geophys. Res.*, **119**, 8255–8270, https://doi.org/10.1002/2014JC010336.

Gnanadesikan, A., and Coauthors, 2006: GFDL's CM2 global coupled climate models. Part II: The baseline ocean simulation. *J. Climate*, **19**, 675–697, https://doi.org/10.1175/JCLI3630.1.

Good, S. A., M. J. Martin, and N. A. Rayner, 2013: EN4: Quality controlled ocean temperature and salinity profiles and monthly objective analyses with uncertainty estimates. *J. Geophys. Res.*, **118**(12), 6704–6716, https://doi.org/10.1002/2013JC009067.

Gouriou, Y., and T. Delcroix, 2002: Seasonal and ENSO variations of sea surface salinity and temperature in the South Pacific Convergence Zone during 1976–2000. *J. Geophys. Res.*, **107**(C12), 8011, http://doi.org/10.1029/2001JC000830.

Griffies, S. M., 2009: Elements of MOM4p1. GFDL Ocean Group Tech. Rep. 6, 377 pp.

Hackert, E., A. J. Busalacchi, and J. Ballabrera-Poy, 2014: Impact of Aquarius sea surface salinity observations on coupled forecasts for the tropical Indo-Pacific Ocean. *J. Geophys. Res.*, **119**, 4045–4067, https://doi.org/10.1002/2013JC009697.

Ham, Y.-G., and J.-S. Kug, 2014: Effects of Pacific Intertropical Convergence Zone precipitation bias on ENSO phase transition. *Environmental Research Letters*, **9**(6), 064008, https://doi.org/10.1088/1748-9326/9/6/064008.

Huang, B. Y., and Coauthors, 2015: Further exploring and quantifying uncertainties for Extended Reconstructed Sea Surface Temperature (ERSST) version 4 (v4). *J. Climate*, **29**, 3119–3142, https://doi.org/10.1175/JCLI-D-15-0430.1.

Hasson, A. E. A., T. Delcroix, and R. Dussin, 2013: An assessment of the mixed layer salinity budget in the tropical Pacific Ocean: Observations and modelling (1990–2009). *Ocean Dynamics*, **63**, 179–194, https://doi.org/10.1007/s10236-013-0596-2.

Katsura, S., E. Oka, B. Qiu, and N. Schneider, 2013: Formation and subduction of North Pacific tropical water and their interannual variability. *J. Phys. Oceanogr.*, **43**, 2400–2415, https://doi.org/10.1175/JPO-D-13-031.1.

Kim, K.-Y., 2002: Investigation of ENSO variability using cyclostationary EOFs of observational data. *Meteor. Atmos. Phys.*, **81**(3–4), 149–168, https://doi.org/10.1007/s00703-002-0549-7.

Kim, K.-Y., and G. R. North, 1997: EOFs of harmonizable cyclostationary processes. *J. Atmos. Sci.*, **54**, 2416–2427, https://doi.org/10.1175/1520-0469(1997)054<2416:EOHCP>2.0.CO;2.

Kim, K.-Y., G. R. North, and J. P. Huang, 1996: EOFs of one-dimensional cyclostationary time series: Computations, examples, and stochastic modeling. *J. Atmos. Sci.*, **53**, 1007–1017, https://doi.org/10.1175/1520-0469(1996)053<1007:EOODCT>2.0.CO;2.

Kim, W., S.-W. Yeh, J.-H. Kim, J.-S. Kug, and M. Kwon, 2011: The unique 2009–2010 El Niño event: A fast phase transition of warm pool El Niño to La Niña. *Geophys. Res. Lett.*, **38**(15), L15809, https://doi.org/10.1029/2011GL048521.

Kug, J.-S., and I.-S. Kang, 2006: Interactive feedback between ENSO and the Indian Ocean. *J. Climate*, **19**(9), 1784–1801, https://doi.org/10.1175/JCLI3660.1.

Langford, S., S. Stevenson, and D. Noone, 2014: Analysis of low-frequency precipitation variability in CMIP5 historical simulations for southwestern North America. *J. Climate*, **27**(7), 2735–2756, https://doi.org/10.1175/JCLI-D-13-00317.1.

Li, G., S.-P. Xie, 2012: Origins of tropical-wide SST biases in CMIP multi-model ensembles. *Geophys. Res. Lett.*, **39**, L22703, https://doi.org/10.1029/2012GL053777.

Li, G., S.-P. Xie, 2014: Tropical biases in CMIP5 multimodel ensemble: The excessive equatorial Pacific cold tongue and double ITCZ problems. *J. Climate*, **27**, 1765–1780, https://doi.org/10.1175/JCLI-D-13-00337.1.

Lin, J.-L., 2007: The double-ITCZ problem in IPCC AR4 Coupled GCMs: Ocean-atmosphere feedback analysis. *J. Climate*, **20**, 4497–4525, https://doi.org/10.1175/JCLI4272.1.

Lin, S.-J., 2004: A "vertically Lagrangian" finite-volume dynamical core for global models. *Mon. Wea. Rev.*, **132**, 2293–2307, https://doi.org/10.1175/1520-0493(2004)132<2293:AVLFDC>2.0.CO;2.

Lukas, R., and E. Lindstrom, 1991: The mixed layer of the western equatorial Pacific Ocean. *J. Geophys. Res.*, **96**, 3343–3357, https://doi.org/10.1029/90JC01951.

Maes, C., K. Ando, T. Delcroix, W. S. Kessler, M. J. McPhaden, and D. Roemmich, 2006: Observed correlation of surface salinity, temperature and barrier layer at the eastern edge of the western Pacific warm pool. *Geophys. Res. Lett.*, **33**(6), L06601, https://doi.org/10.1029/2005gl024772.

Mignot, J., C. de Boyer Montégut, A. Lazar, and S. Cravatte, 2007: Control of salinity on the mixed layer depth in the world ocean: 2. Tropical areas. *J. Geophys. Res.*, **112**(C10), C10010, https://doi.org/10.1029/2006JC003954.

Picaut, J., M. Ioualalen, C. Menkes, T. Delcroix, and M. J.

McPhaden, 1996: Mechanism of the zonal displacements of the Pacific warm pool: Implications for ENSO. *Science*, **274**(5292), 1486–1489, https://doi.org/10.1126/science.274.5292.1486.

Picaut, J., M. Ioualalen, T. Delcroix, F. Masia, R. Murtugudde, and J. Vialard, 2001: The oceanic zone of convergence on the eastern edge of the Pacific warm pool: A synthesis of results and implications for El Niño-Southern Oscillation and biogeochemical phenomena. *J. Geophys. Res*., **106**(C2), 2363–2386, https://doi.org/10.1029/2000JC900141.

Ponte, R. M., and N. T. Vinogradova, 2016: An assessment of basic processes controlling mean surface salinity over the global ocean. *Geophys. Res. Lett*., **43**, 7052–7058, https://doi.org/10.1002/2016GL069857.

Qu, T. D., S. Gao, and R. A. Fine, 2013: Subduction of south pacific tropical water and its equatorward pathways as shown by a simulated passive tracer. *J. Phys. Oceanogr*., **43**, 1551–1565, https://doi.org/10.1175/JPO-D-12-0180.1.

Qu, T. D., Y. T. Song, and C. Maes, 2014: Sea surface salinity and barrier layer variability in the equatorial Pacific as seen from Aquarius and Argo. *J. Geophys. Res*., **119**(1), 15–29, https://doi.org/10.1002/2013JC009375.

Ren, L., and S. C. Riser, 2009: Seasonal salt budget in the northeast Pacific Ocean. *J. Geophys. Res*., **114**, C12004, https://doi.org/10.1029/2009JC005307.

Schmitt, R. W., 1990: On the density ratio balance in the central water. *J. Phys. Oceanogr*., **20**(6), 900–906, https://doi.org/10.1175/1520-0485(1990)020<0900:OTDRBI>2.0.CO;2.

Shevliakova, E., and Coauthors, 2009: Carbon cycling under 300 years of land use change: Importance of the secondary vegetation sink. *Global Biogeochemical Cycles*, **23**, GB2022, https://doi.org/10.1029/2007GB003176.

Singh, A., T. Delcroix, and S. Cravatte, 2011: Contrasting the flavors of El Niño-Southern Oscillation using sea surface salinity observations. *J. Geophys. Res*., **116**(C6), C06016, https://doi.org/10.1029/2010jc006862.

Skliris, N., R. Marsh, S. A. Josey, S. A. Good, C. L. Liu, and R. P. Allan, 2014: Salinity changes in the World Ocean since 1950 in relation to changing surface freshwater fluxes. *Climate Dyn*., **43**, 709–736, https://doi.org/10.1007/s00382-014-2131-7.

Sprintall, J., and M. Tomczak, 1992: Evidence of the barrier layer in the surface layer of the tropics. *J. Geophys. Res*., **97**, 7305–7316, https://doi.org/10.1029/92JC00407.

Taylor, K. E., R. J. Stouffer, and G. A. Meehl, 2012: An overview of CMIP5 and the experiment design. *Bull. Amer. Meteor. Soc*., **93**, 485–498, https://doi.org/10.1175/BAMS-D-11-00094.1.

Terray, L., L. Corre, S. Cravatte, T. Delcroix, G. Reverdin, and A. Ribes, 2012: Near-surface salinity as nature's rain gauge to detect human influence on the tropical water cycle. *J. Climate*, **25**, 958–977, https://doi.org/10.1175/JCLI-D-10-05025.1.

Vialard, J., and P. Delecluse, 1998: An OGCM study for the TOGA decade. Part I: Role of salinity in the physics of the western Pacific fresh pool. *J. Phys. Oceanogr*., **28**, 1071–1088, https://doi.org/10.1175/1520-0485(1998)028<1071:AOSFTT>2.0.CO;2.

Vialard, J., P. Delecluse, and C. Menkes, 2002: A modeling study of salinity variability and its effects in the tropical Pacific Ocean during the 1993–1999 period. *J. Geophys. Res*., **107**(C12), 8005, https://doi.org/10.1029/2000JC000758.

Vinogradova, N. T., and R. M. Ponte, 2013: Clarifying the link between surface salinity and freshwater fluxes on monthly to interannual time scales. *J. Geophys. Res*., **118**, 3190–3201, https://doi.org/10.1002/jgrc.20200.

Webster, P. J., 1994: The role of hydrological processes in ocean-atmosphere interactions. *Rev. Geophys*., **32**, 427–476, https://doi.org/10.1029/94RG01873.

Winton, M., 2000: A reformulated three-layer sea ice model. *J. Atmos. Oceanic Technol*., **17**, 525–531, https://doi.org/10.1175/1520-0426(2000)017<0525:ARTLSI>2.0.CO;2.

Yan, Y. F., L. Li, and C. Z. Wang, 2017a: The effects of oceanic barrier layer on the upper ocean response to tropical cyclones. *J. Geophys. Res*., **122**, 4829–4844, https://doi.org/10.1002/2017JC012694.

Yan, Y. F., D. Z. Xu, K. Yu, and Y. Q. Qi, 2017b: Propagation of the subsurface freshening water and its major source in the northwestern Pacific. *J. Geophys. Res*., **122**, 6857–6871, https://doi.org/10.1002/2017JC013033.

Yeo, S.-R., and K.-Y. Kim, 2014: Global warming, low-frequency variability, and biennial oscillation: An attempt to understand the physical mechanisms driving major ENSO events. *Climate Dyn*., **43**, 771–786, https://doi.org/10.1007/s00382-013-1862-1.

Yim, B. Y., S.-W. Yeh, Y. Noh, B.-K. Moon, and Y.-G. Park, 2008: Sea surface salinity variability and its relation to El Niño in a CGCM. *Asia-Pacific Journal of the Atmospheric Sciences*, **44**, 173–189.

Yoo, S.-H., J. Fasullo, S. Yang, and C.-H. Ho, 2010: On the relationship between Indian Ocean sea surface temperature and the transition from El Niño to La Niña. *J. Geophys. Res*., **115**, D15114, https://doi.org/10.1029/2009JD012978.

Yu, L. S., 2011: A global relationship between the ocean water cycle and near-surface salinity. *J. Geophys. Res*., **116**, C10025, https://doi.org/10.1029/2010JC006937.

Yu, L. S., and R. A. Weller, 2007: Objectively analyzed air-sea heat fluxes for the global ice-free oceans (1981–2005). *Bull. Amer. Meteor. Soc*., **88**, 527–539, https://doi.org/10.1175/BAMS-88-4-527.

Yu, Y. Q., L. Chen, and Y. L. Zhang, 2014: ENSO and PDO in two versions of FGOALS. Flexible Global Ocean-Atmosphere-Land System Model, T. Zhou et al., Eds., Springer, Berlin, Heidelberg, 107–113, https://doi.org/10.1007/978-3-642-41801-3_14.

Zhang, R.-H., and A. J. Busalacchi, 2009: Freshwater flux (FWF)-induced oceanic feedback in a hybrid coupled model of the tropical Pacific. *J. Climate*, **22**, 853–879, https://doi.org/10.1175/2008JCLI2543.1.

Zhang, R.-H., A. J. Busalacchi, R. G. Murtugudde, P. A. Arkin, and J. Ballabrera-Poy, 2006: An empirical parameterization for the salinity of subsurface water entrained into the ocean mixed layer (S_e) in the tropical Pacific. *Geophys. Res. Lett*., **33**(2), L02605, https://doi.org/10.1029/2005GL024218.

Zhang, R.-H., G. H. Wang, D. K. Chen, A. J. Busalacchi, and E. C. Hackert, 2010: Interannual biases induced by freshwater flux and coupled feedback in the tropical Pacific. *Mon. Wea. Rev*., **138**, 1715–1737, https://doi.org/10.1175/2009MWR3054.1.

Zhang, R.-H, F. Zheng, J. S. Zhu, Y. H. Pei, Q. A. Zheng, and Z. G. Wang, 2012: Modulation of El Niño-Southern Oscillation by freshwater flux and salinity variability in the tropical Pacific. *Adv. Atmos. Sci.*, **29**(4), 647–660, https://doi.org/10.1007/s00376-012-1235-4.

Zhang, R. -H., C. Gao, X. B. Kang, H. Zhi, Z. G. Wang, and L. C. Feng, 2015: ENSO modulations due to interannual variabil-

ity of freshwater forcing and ocean biology-induced heating in the tropical Pacific. *Scientific ReportsSci. Rep.*, **5**, 18506; https://doi.org/10.1038/srep18506.

Zheng, F., and R.-H. Zhang, 2012: Effects of interannual salinity variability and freshwater flux forcing on the development of the 2007/08 La Niña event diagnosed from Argo and satellite data. *Dyn. Atmos. Oceans*, **57**, 45–57, https://doi.org/10.1016/j.dynatmoce.2012.06.002.

Zheng, F., R.-H. Zhang, and J. Zhu, 2014: Effects of interannual salinity variability on the barrier layer in the western-central equatorial Pacific: A diagnostic analysis from Argo. *Adv. Atmos. Sci.*, **31**(3), 532–542, https://doi.org/10.1007/s00376-013-3061-8.

Zhi, H., R.-H. Zhang, P. F. Lin, and L. N. Wang, 2015: Quantitative analysis of the feedback induced by the freshwater flux in the tropical Pacific using CMIP5. *Adv. Atmos. Sci.*, **32**(10), 1341–1353, https://doi.org/10.1007/s00376-015-5064-0.

Zhu, J. S., and Coauthors, 2014: Salinity anomaly as a trigger for ENSO events. *Scientific Reports*, **4**, 6821, https://doi.org/10.1038/srep06821.